

A robust baro-radar-inertial odometry m-estimator for multicopter navigation in cities and forests

Rik Girod¹, Marco Hauswirth¹, Patrick Pfreundschiuh¹, Mariano Biasio¹, and Roland Siegwart¹

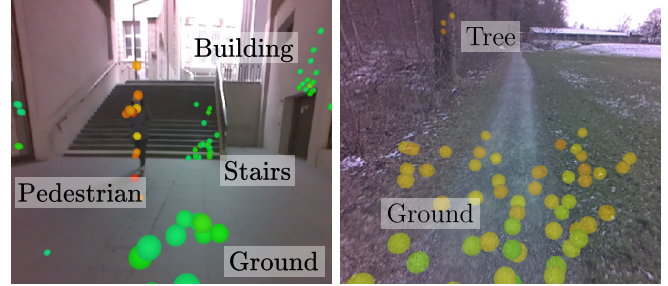
Abstract—Search and rescue operations require mobile robots to navigate unstructured indoor and outdoor environments. In particular, actively stabilized multirotor drones need precise movement data to balance and avoid obstacles. Combining radial velocities from on-chip radar with MEMS inertial sensing has proven to provide robust, lightweight, and consistent state estimation, even in visually or geometrically degraded environments. Statistical tests robustify these estimators against radar outliers. However, available work with binary outlier filters lacks adaptability to various hardware setups and environments. Other work has predominantly been tested in handheld static environments or automotive contexts. This work introduces a robust baro-radar-inertial odometry (BRIO) m-estimator for quadcopter flights in typical GNSS-denied scenarios. Extensive real-world closed-loop flights in cities and forests demonstrate robustness to moving objects and ghost targets, maintaining a consistent performance with 0.5% to 3.2% drift per distance traveled. Benchmarks on public datasets validate the system’s generalizability. The code, dataset, and video are available at <https://github.com/ethz-asl/rio>.

I. INTRODUCTION

Mobile robots are actively researched for disaster response. Small, multirotor uncrewed aerial vehicles (UAVs) are ideal for exploration as they can traverse rubble and obstacles [1]. In confined spaces UAVs need onboard positioning to correct inertial measurement unit (IMU) drift. Vision, lidar, and thermal navigation solutions have been proposed [2, 3, 4], but these are vulnerable to visual degradation, geometric ambiguity, or weak temperature gradients.

With the availability of automotive single-chip frequency-modulated continuous-wave (FMCW) radars [5], Doer and Trommer [6] demonstrated the first radar-inertial-stabilized quadcopter flights. Due to its active sensing principle, radar is robust to visual degradation, such as darkness or fog. Further, radar’s ability to measure linear displacements and IMU’s ability to measure orientation changes make them an outstanding sensor combination to estimate the standard navigation state of position, velocity, and orientation. This work considers the fusion of bearing Doppler radar detections with IMU measurements.

A core assumption in our work and others is that all radar detections are static. However, moving objects and singular ghost targets introduced by multipath propagations or electromagnetic noise often violate this assumption. Fig. 1a shows that these outliers have a radial velocity inconsistent with the robot movement, and thus, statistical outlier tests



(a) Urban environment hovering. (b) Forest path forward flight.

Fig. 1: Onboard view from our radar-stabilized quadcopter. The points show 1 s accumulated, overlaid radar detections colored by their radial velocity (green: zero, orange: towards the radar, blue: away from the radar).

robustify a radar-inertial odometry (RIO) estimator. Our work shows robust optimization sufficiently suppresses noise across realistic environments. In contrast to binary outlier rejection, e.g., RANSAC, m-estimation requires only a single tuning parameter.

A second necessity for estimating body motion is at least three radar detections with linearly independent direction-of-arrival (DoA). Our experiments show that sufficient independent detections are generally given across human-made and natural environments. The estimation is always stable, even in scenes where the bearing angle distribution is ill-conditioned, such as the dense ground reflections in Fig. 1b.

Finally, the DoA may be biased, causing drift, especially in the gravity-affected elevation direction. Differential barometry efficiently mitigates vertical drift. Robust optimization also helps to reject noise induced by propeller downwash.

This work presents an experimental validation of BRIO for quadcopter navigation in urban and natural environments. It derives a factor-graph m-estimator with robust bearing Doppler and differential pressure factors. Extensive experiments show estimator robustness against common outliers, such as cyclists, pedestrians, streetcars, multipath detections, and aerodynamic effects. The estimated trajectory shows low drift and sufficient smoothness for multirotor feedback control. Summarized, our contributions are

- A BRIO m-estimator with robust bearing Doppler, robust differential barometry, and zero-velocity factors.
- Experimental tuning, robustness and performance analysis through radar-stabilized quadcopter flights in realistic natural and human-made environments.
- Demonstrating generalizability and state-of-the-art performance on a public dataset benchmark.
- Open-source estimator, sensor drivers, and dataset.

*This work was supported by Armasuisse S+T.

¹Authors are with Autonomous Systems Lab, ETH Zürich, 8092 Zürich, Switzerland {brik, haumarco, patripfr, mbiasio, rsiegwart}@ethz.ch

II. RELATED WORK

Yokoo et al. [7] introduced the idea of pose estimation from sparse FMCW radar bearing Doppler and IMU measurements. Consequently, Kellner et al. [8] showed that cost-efficient, single-chip FMCW radar delivers ego-motion estimation for autonomous driving. They showed that two linearly independent radial velocity measurements are sufficient to compute a car’s linear velocity.

Doer and Trommer [6] generalized this concept to three-dimensional navigation. They introduced a navigation filter combining IMU and barometry with linear velocities computed from at least three radial velocities and least squares. However, their binary radar outlier tests require 16 tuning parameters, complication setup adaptation. Their barometry neglects aerodynamic disturbances and bias observability.

Their follow-up work uses multiple radars and introduces yaw estimation through a Manhattan world assumption [9]. Their results with additional sensors are mixed, and the assumption is unsuited for natural environments. Instead, our results show sufficient yaw accuracy can be achieved on a consumer-grade IMU using turn-on-bias calibration.

Huang et al. [10] examine how radar resolution affects state estimation accuracy. A robust optimization computes the linear velocity from multiple radar detections and extracts the covariance. A sliding window estimator fuses it with IMU data. Our experiments show that a simpler single radar-baro setup provides competitive performance and smooth state estimation for aerial robots in real-world environments.

Michalczyk et al. [11] combine instantaneous radar velocity updates with radar landmark tracking in a filter framework. The follow-up work achieves a drift between 0.17% to 1.62% [12]. However, feature tracking and mapping add complexity and are a source of error [13]. In particular, generalizing feature association is challenging due to the fluctuating nature of radar reflections [14, pp. 106-108]. Michalczyk et al. [12] only present results in a small lab environment with artificially placed corner reflectors. We limit tracking to static scenes to detect standstill. Thus, we avoid restrictive radar target assumptions. Our approach has similar accuracy while showing broader applicability.

Kramer and Heckman [15] present a fixed-lag smoother, similar to a total least squares problem. They co-estimate robot velocity, orientation, radar detection DoA, and Doppler velocity. However, to stabilize the optimizer, they require MLESAC prefiltering on top of robust loss. Our approach considers radar reflections fixed, has fewer optimization variables, and does not require prefiltering.

Kramer et al. [16] work is closest to our approach. They directly fuse individual bearing Doppler measurements in a robust optimization using Cauchy loss to reject radar outliers. However, our work goes far beyond their work. We compare different loss functions and demonstrate robust barometer fusion, closed-loop quadrotor control, robustness to dynamic objects, position estimation, turn-on-bias calibration, and zero-velocity tracking. Our work is available as open-source.

Finally, multiple radar state estimation approaches tailored for ground robots exist [17]. However, most, such as full

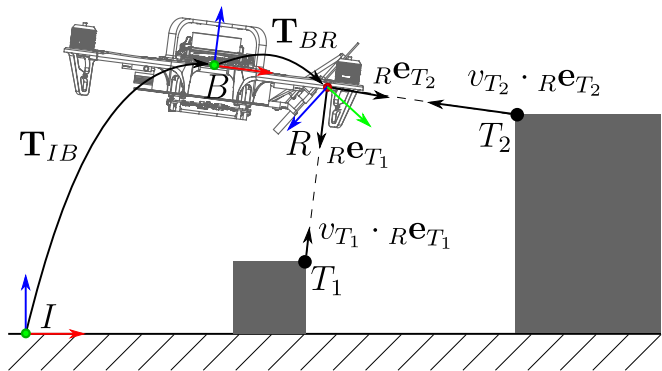


Fig. 2: Quadcopter side view with coordinate frames and two radar detections.

SLAM pipelines or large spinning radars on autonomous cars, are unsuited for quadcopter control, which requires lightweight velocity estimation and not a dense map.

III. NOTATION

Capital letters denote right-handed coordinate frames. The origin of a specific coordinate frame is denoted by the same letter. Matrices and vectors are bold. $A\mathbf{t}_{BC}$ is the vector from source B to target C , expressed in coordinate frame A . $A\mathbf{e}_B \in S^2$ is the unit vector on the 2-sphere pointing from the origin of coordinate frame A towards location B .

The direction cosine matrix $\mathbf{R}_{AB} \in SO(3)$ represent a rotation and maps vector $B\mathbf{t}_{AB}$ from frame B to frame A .

$$A\mathbf{t}_{AB} = \mathbf{R}_{AB} \cdot B\mathbf{t}_{AB} \quad (1)$$

Consequently, a rotation \mathbf{R}_{AC} can be expressed by

$$\mathbf{R}_{AC} = \mathbf{R}_{AB}\mathbf{R}_{BC}. \quad (2)$$

A rigid transformation $\mathbf{T}_{AB} \in SE(3)$ is a composition of the rotation $\mathbf{R}_{AB} \in SO(3)$ and translation $A\mathbf{t}_{AB} \in \mathbb{R}^3$.

IV. RADAR-INERTIAL STATE ESTIMATION

The system is described by the three coordinate frames, denoted by capital letters I , B , and R in Fig. 2. The unit vectors $I\mathbf{e}_x$, $I\mathbf{e}_y$, $I\mathbf{e}_z$ define the inertial frame I , where $I\mathbf{e}_x$ and $I\mathbf{e}_y$ span a plane tangential to the earth ellipsoid and $I\mathbf{e}_z$ points up. B denotes the body frame which coincides with the IMU axes with $B\mathbf{e}_x$ forward, $B\mathbf{e}_y$ left, and $B\mathbf{e}_z$ up. R is the radar frame, where $R\mathbf{e}_x$ points at positive azimuth direction, $R\mathbf{e}_y$ at boresight, and $R\mathbf{e}_z$ at positive elevation direction. The coordinate frames are linked by rigid transformation \mathbf{T}_{IB} and \mathbf{T}_{BR} . \mathbf{T}_{IB} is the online estimated, time-varying robot pose. \mathbf{T}_{BR} is the extrinsic calibration between IMU and radar and obtained from CAD.

A. System State

The IMU pose $\mathbf{T}_{IB}^i \in SE(3)$, composed of orientation $\mathbf{R}_{IB}^i \in SO(3)$ and translation $I\mathbf{t}_{IB}^i \in \mathbb{R}^3$, the body velocity $I\mathbf{v}_{IB}^i \in \mathbb{R}^3$, the gyroscope biases $B\mathbf{b}_g^i \in \mathbb{R}^3$, and the accelerometer biases $B\mathbf{b}_a^i \in \mathbb{R}^3$ form the 15-dimensional state \mathbf{x} at time i . Our framework also tracks the location of zero velocity radar detections \mathbf{t}^j with track index j , where

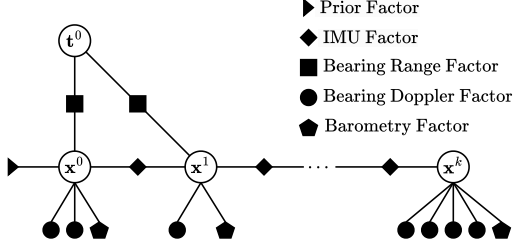


Fig. 3: Factor graph representation with two, one, and four Doppler measurements and a zero-velocity landmark observed from the first and second state.

$I\mathbf{t}_{IT}^{i,m}$ is the estimated position of the m -th radar detection observed at time i , tracked over multiple frames $\mathcal{K}_j \subseteq \mathcal{K}_k$.

$$\mathbf{x}^i = [\mathbf{R}_{IB}^i, I\mathbf{v}_{IB}^i, I\mathbf{v}_{IB}^i, B\mathbf{b}_g^i, B\mathbf{b}_a^i]^T \quad \mathbf{t}^j = [I\mathbf{t}_{IT}^{j,m}]^T \quad (3)$$

The estimator creates a new state with each radar frame. \mathcal{X}_k is the set of all estimated states with \mathcal{K}_k the set of all radar frames up to time k . Analogously, \mathcal{T}_k is the set of all estimated zero velocity detection positions with \mathcal{L}_k the set of all tracks up to time k .

$$\mathcal{X}_k = \{\mathbf{x}^i\}_{i \in \mathcal{K}_k} \quad \mathcal{T}_k = \{\mathbf{t}^j\}_{j \in \mathcal{L}_k} \quad (4)$$

B. Measurements

The inputs to our system are bearing Doppler radar detections, IMU measurements, and optionally barometric pressure. We denote \mathcal{R}^i as the set of all detections at time i . $\mathcal{I}^{i,i+1}$ is the set of IMU measurements between radar frame i and $i+1$. \mathcal{B}^i is the pressure measurement closest to time i . The measurement set up to time k is

$$\mathcal{Z}_k = \{\mathcal{R}^i, \mathcal{I}^{i,i+1}, \mathcal{B}^i\}_{(i,i+1) \in \mathcal{K}_k}. \quad (5)$$

C. Optimization Criterion

The online estimator evaluates the maximum a posteriori probability (MAP) of states \mathcal{X}_k and zero-velocity tracks \mathcal{T}_k given all available observations \mathcal{Z}_k .

$$\mathcal{X}_k^{\text{MAP}} = \arg \max_{\mathcal{X}_k, \mathcal{T}_k} p(\mathcal{X}_k, \mathcal{T}_k | \mathcal{Z}_k) \quad (6)$$

The factor graph in Fig. 3 represents the unnormalized posterior [18].

$$\begin{aligned} \mathcal{X}_k^{\text{MAP}} = \arg \min_{\mathcal{X}_k, \mathcal{T}_k} & \underbrace{\|\mathbf{r}_P^0\|_{\Sigma_P}^2}_{(\text{prior})} + \sum_{(i,i+1) \in \mathcal{K}_k} \underbrace{\|\mathbf{r}_I^{i,i+1}\|_{\Sigma_I}^2}_{(\text{IMU})} \\ & + \sum_{j \in \mathcal{L}_k} \sum_{i \in \mathcal{K}_j} \underbrace{\|\mathbf{r}_T^{i,j}\|_{\Sigma_T}^2}_{(\text{zero-velocity track})} \\ & + \sum_{i \in \mathcal{K}_k} \sum_{m \in \mathcal{R}^i} \underbrace{\rho \left(\frac{\|r_D^{i,m}\|}{\sigma_D} \right) \|r_D^{i,m}\|_{\Sigma_D}^2}_{(\text{robust bearing Doppler})} \\ & + \sum_{i \in \mathcal{K}_k} \underbrace{\rho \left(\frac{\|r_B^i\|}{\sigma_B} \right) \|r_B^i\|_{\Sigma_B}^2}_{(\text{robust barometry})}, \end{aligned} \quad (7)$$

where \mathbf{r}_P are prior, \mathbf{r}_I IMU, \mathbf{r}_T zero-velocity track, r_D bearing Doppler, and r_B barometry factor residual errors. $\Sigma_P, \Sigma_I, \Sigma_T, \Sigma_D, \Sigma_B, \sigma_D$, and σ_B are the corresponding measurement covariances respectively standard deviations. $\|\epsilon\|_{\Sigma}^2 = \epsilon^T \Sigma^{-1} \epsilon$ is the squared Mahalanobis distance with covariance Σ . ρ is a robust loss function specified in Sections IV-D and IV-E.

D. Robust bearing Doppler Factor

We consider FMCW radar with a standard detection processing chain. Upon receiving an asynchronous triggering signal, the multiple-input and multiple-output (MIMO) radar emits a predefined FMCW chirp sequence. The returning analog signal is mixed with the transmitting signal, converted to digital, windowed, range, and Doppler processed, constant false alarm rate (CFAR) filtered, and DoA processed. The CFAR detection extracts strong reflections separated in the range-Doppler space. CFAR detection is an efficient data reduction step as DoA processing and data transfer to the host computer only need to be done on a few data points. Also, the CFAR effectively filters reflections from noise.

The result is a sparse pointcloud with detections \mathcal{R}^i at time $i \in \mathcal{K}_k$. Detection $T^{i,m} \in \mathcal{R}^i$ contains direction-of-arrival $R\mathbf{e}_T^{i,m} = \frac{R\mathbf{r}_{RT}^{i,m}}{\|R\mathbf{r}_{RT}^{i,m}\|}$, Doppler velocity $v_T^{i,m}$, range $r_{T_m}^i = \|R\mathbf{r}_{RT}^{i,m}\|$, signal-to-noise ratio (SNR) $\text{SNR}_T^{i,m}$, and noise $w_T^{i,m}$. Fig. 1 shows these detections mostly occur on geometric edges and strong changes in relative permittivity, e.g., from air to metal on the window frame. We use the DoA and Doppler velocity to constrain the body velocity into the direction of the detection as indicated in Fig. 2.

The bearing Doppler residual $r_D^{i,m}$ is the difference between the estimated radar linear velocity $R\mathbf{v}_{IR}^i$ projected onto the detection direction and the measured Doppler. It depends on the state variables $\mathbf{R}_{IB}^i, I\mathbf{v}_{IB}^i$, and $B\mathbf{b}_g^i$, radar measurements $R\mathbf{e}_T^{i,m}$ and $v_T^{i,m}$, and angular velocity $B\boldsymbol{\omega}_{IB}^i$.

$$r_D^{i,m} = - (R\mathbf{v}_{IR}^i)^T \cdot R\mathbf{e}_T^{i,m} - v_T^{i,m} \quad (8)$$

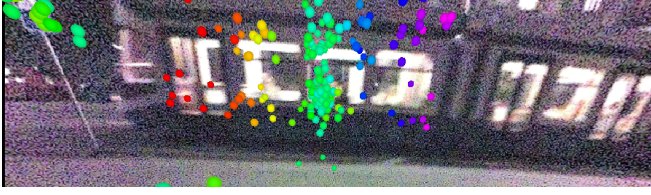
$$= - \left((\mathbf{R}_{IB}^i \mathbf{R}_{BR})^T \cdot I\mathbf{v}_{IR}^i \right)^T \cdot R\mathbf{e}_T^{i,m} - v_T^{i,m}, \quad (9)$$

with the radar velocity $I\mathbf{v}_{IR}^i$ derived from the body velocity.

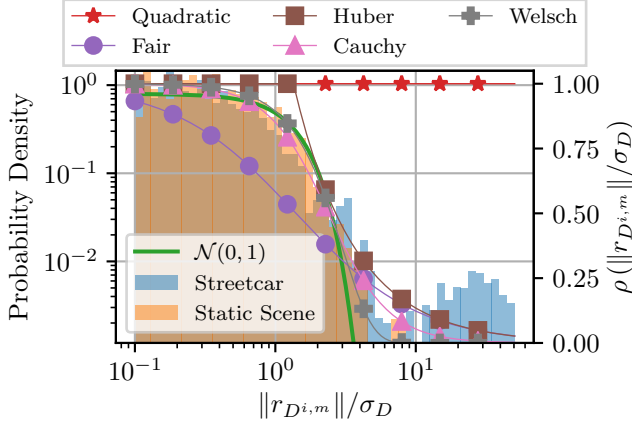
$$I\mathbf{v}_{IR}^i = I\mathbf{v}_{IB}^i + \mathbf{R}_{IB}^i \left((B\boldsymbol{\omega}_{IB}^i - B\mathbf{b}_g^i) \times B\mathbf{t}_{BR} \right) \quad (10)$$

In a static scene, the bearing Doppler residual noise is normally distributed with standard deviation σ_D as shown in Fig. 4b. However, the radar occasionally detects ghost targets or moving objects, creating long-tailed residual noise. For example, the streetcar in Fig. 4a generates approaching (orange/red) and receding (blue/purple) radial velocity outliers. Fig. 4b shows the corresponding bearing Doppler residual error distribution with a visible outlier set located between 10 to 50 standard deviations. The following evaluated loss functions [19] suppress these outliers to varying degrees.

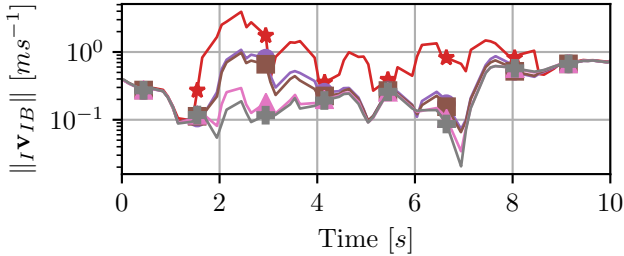
Our experiments with moving objects have shown that a loss function should be selected where the weighting function ρ approaches zero. Fig. 4c shows the velocity estimate during hover while the streetcar passes. The estimate should be



(a) Quadcopter onboard view. Streetcar passing from left to right.



(b) Normalized absolute bearing Doppler pre-fit residuals across one optimization window with and without moving object in the radar field of view. $\sigma_D = 0.05$, and optimizer using Welsch loss. Robust loss functions tuned to 95% asymptotic efficiency [19].



(c) Estimated body velocity while hovering in front of the streetcar.

Fig. 4: Robust bearing Doppler loss function analysis based on streetcar passing hovering quadcopter. Radar detections accumulated over 10 s optimization window.

close to zero. A pure quadratic loss causes significant non-zero velocity estimates. Also, Fair and Huber’s losses are insufficient to suppress the streetcar detections. Even Cauchy loss will still predict some movement in the presence of outliers. Welsch loss shows the steadiest hover estimate and is selected for the estimation problem (7).

One beauty of using only robust loss for outlier rejection compared to additional statistical tests, such as RANSAC, is that only σ_D requires tuning to normalize the residuals (7). We keep σ_D constant throughout all experiments. We did not observe instabilities in the optimization with any of the evaluated ρ functions.

E. Robust Barometric Factor

In principle, the radar factor is sufficient to observe the body velocity and integrated position if three linearly independent radial velocities are measured. However, systematic

bias in these measurements, paired with errors in the extrinsic calibration, gravity constant, and IMU biases, cause altitude estimation drift. To compensate for errors in height, we measure differential barometry. The barometer residual r_B^i is the difference between estimated height, offset by bias z_p^0 , and measured height z_p^i .

$$r_B^i = r e_z^T \cdot I \mathbf{t}_{IB}^i + z_p^0 - z_p^i, \quad (11)$$

with z_p^i a function of the pressure p^i at time i , derived from an earth atmosphere model [20].

$$z_p^i = \frac{288.08 \left(\frac{p^i}{101290} \right)^{\frac{1}{5.256}} - 273.1 - 15.04}{-0.00649} \quad (12)$$

Barometric measurements are biased by ambient temperature changes [21]. Unlike Doer and Trommer [6], who co-estimate the pressure bias z_p^0 , we set it constant using the first barometer measurement. We noticed that z_p^0 is unobservable because the ambient pressure drift due to weather changes is much smaller than the RIO height estimation drift.

However, our estimator is robust to sudden disturbances, such as ground effects during touch-down (Fig. 5a). Without suppression, this noise can falsely deviate the vertical velocity estimate, as seen in red in Fig. 5b. The Fair robust loss function ensures a smooth estimate. Apart from these few aerodynamic occasions, the barometric residuals are normally distributed as shown in Fig. 5c.

F. Zero-Velocity Detection Tracking

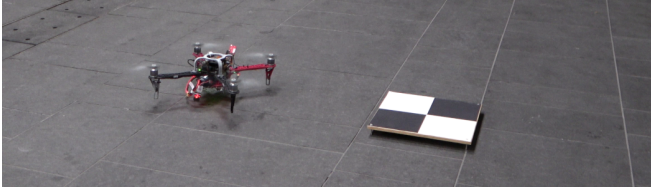
Before take-off and after landing, all static reflections have zero Doppler velocity and cannot be separated in Doppler space by the CFAR detector. Thus, the radar point cloud often consists of only one or two targets, representing the strongest reflections that can be separated by range. This is insufficient to compute the linear body velocity, so the state estimate will drift on a sphere or circle. Since the environment and robot are static, consecutive reflections are identical within the sensor resolution. We track these targets, making the full state observable at zero velocity.

Let $T^{i,m} \in \mathcal{R}^i$ be detection m at time i and $T^{i,\underline{m}} \in \mathcal{R}^i$ be detection \underline{m} at time i . Tracks are discarded after being unobserved for a fixed amount of radar frames. Targets are associated if they have identical measurements.

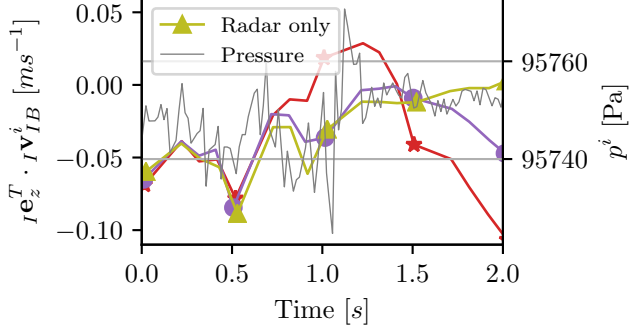
$$\begin{aligned} & \left({}_R \mathbf{t}_{RT}^{i,m} = {}_R \mathbf{t}_{RT}^{i,\underline{m}} \right) \wedge \left(v_T^{i,m} = v_T^{i,\underline{m}} = 0 \right) \wedge \\ & \left(\text{SNR}_T^{i,m} = \text{SNR}_T^{i,\underline{m}} \right) \wedge \left(w_T^{i,m} = w_T^{i,\underline{m}} \right) \\ & \Rightarrow T^{i,m} = T^{i,\underline{m}} \end{aligned} \quad (13)$$

The optimizer estimates the position of each track in the inertial frame. The residual, when represented in Cartesian coordinates, is the difference between the estimated detection position \mathbf{t}^j and the measured detection position ${}_R \mathbf{t}_{RT}^{i,m}$. The estimated detection location is transformed from the inertial to the radar frame.

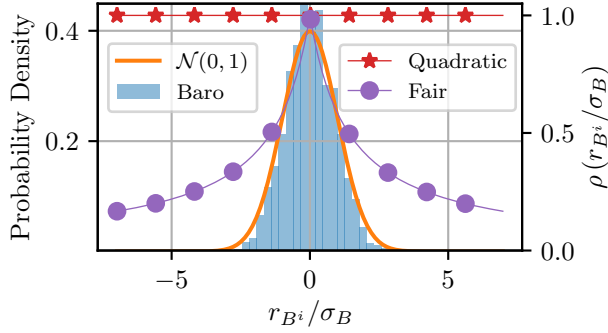
$$\mathbf{r}_T^{i,j} = \left(\mathbf{R}_{IB}^i \mathbf{R}_{BR} \right)^T \left(\mathbf{t}^j - I \mathbf{t}_{IB}^i - \mathbf{R}_{IB}^i \cdot \mathbf{b}_{BR} \right) - {}_R \mathbf{t}_{RT}^{i,m} \quad (14)$$



(a) Photo of quadcopter landing next to take off location.



(b) Vertical velocity estimate during landing at 1s with quadratic and Fair loss. Pressure showing ground effect.



(c) Normalized barometer pre-fit residual distribution over complete flight with $\sigma_B = 0.2$, and Fair barometer residual loss. Robust loss functions tuned to 95% asymptotic efficiency [19]

Fig. 5: Barometer noise and robust loss analysis.

G. IMU Factor

Integrating high-rate IMU measurements as individual factors quickly increases variables in the optimization, making it computationally intractable. Forster et al. [22] presented a method to preintegrate a set of IMU measurements into a single factor. The method successively computes the relative change in orientation, velocity, position. The combined IMU residual between two states is

$$\mathbf{r}_I^{i,i+1} = \left[\mathbf{r}_{\Delta \mathbf{R}_{IB}^{i,i+1}}, \mathbf{r}_{\Delta \mathbf{t}_{IB}^{i,i+1}}, \mathbf{r}_{\Delta \mathbf{v}_{IB}^{i,i+1}}, \mathbf{r}_{\Delta \mathbf{b}_g^{i,i+1}}, \mathbf{r}_{\Delta \mathbf{b}_a^{i,i+1}} \right]. \quad (15)$$

H. Prior Factor

Proper optimizer initialization ensures a consistent state estimate from the start. The yaw bias and orientation require special handling. Observing yaw bias is difficult due to the small lever arm ${}_B \mathbf{t}_{BR}$ and relatively large radar noise σ_D [9]. We calibrate the gyroscope bias by averaging the first messages and initializing it with high certainty. A parallel

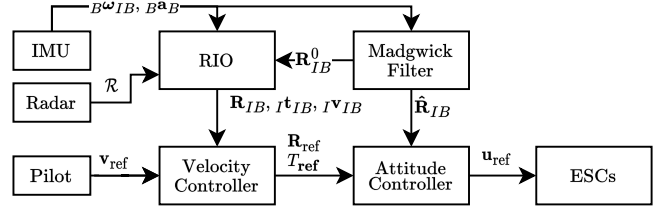


Fig. 6: Quadcopter state estimation and controller diagram.

Madgwick filter [23] aligns orientation with the attitude controller (Fig. 6). All other values are initialized to zero.

$$\mathbf{r}_{\mathbf{R}_{IB}}^0 = \text{Log} \left(\left(\mathbf{R}_{IB}^0 \right)^T \tilde{\mathbf{R}}_{IB}^0 \right) \quad (16)$$

$$\mathbf{r}_{I \mathbf{t}_{IB}}^0 = I \mathbf{t}_{IB}^0 - I \tilde{\mathbf{t}}_{IB}^0 \quad (17)$$

$$\mathbf{r}_{I \mathbf{v}_{IB}}^0 = I \mathbf{v}_{IB}^0 - I \tilde{\mathbf{v}}_{IB}^0 \quad (18)$$

$$\mathbf{r}_{B \mathbf{b}_g}^0 = B \mathbf{b}_g^0 - B \tilde{\mathbf{b}}_g^0 \quad (19)$$

$$\mathbf{r}_{B \mathbf{b}_a}^0 = B \mathbf{b}_a^0 - B \tilde{\mathbf{b}}_a^0, \quad (20)$$

with the logarithmic map transforming a rotation to its tangent space [24] and tilde denoting initial values. The combined prior factor is

$$\mathbf{r}_P^0 = \left[\mathbf{r}_{\mathbf{R}_{IB}}^0, \mathbf{r}_{I \mathbf{t}_{IB}}^0, \mathbf{r}_{I \mathbf{v}_{IB}}^0, \mathbf{r}_{B \mathbf{b}_g}^0, \mathbf{r}_{B \mathbf{b}_a}^0 \right]. \quad (21)$$

V. EXPERIMENTS

We evaluate our approach with radar-stabilized quadcopter flights. The pilot gives velocity setpoints via RC, and if no input is given, the drone hovers stably. Controller, state estimation, and logging run onboard a Nvidia Jetson Orin NX, communicating with a BMI088 IMU, a AWR1843AOPEVM radar, a BMP390 barometer, and ESCs through Linux user space drivers and ROS middleware (Fig. 6). The optimization, implemented with GTSAM [25], runs in two threads using the iSAM2 solver [26]. An optimization thread solves the MAP with a 10s data window typically within 40ms upon radar measurement arrival. A navigation thread outputs the latest state prediction at IMU rate to the controller [27].

The IMU is tuned to capture the drone dynamics but digitally filter as much noise as possible. The accelerometer has a range of 6g, 4-fold oversampling, and 400Hz rate. The synchronized gyroscope has a range of 250°s^{-1} , and a 47Hz low-pass filter. The radar maximizes velocity resolution at 0.04 m s^{-1} , with 2.56 m s^{-1} maximum radial velocity and 10.95m maximum range. The CFAR detection threshold is 15dB for normally distributed residuals. Radar frames are asynchronously triggered at 8Hz. The barometer runs asynchronously at 50Hz with 8-fold oversampling and a cumulative average filter with window size 3. Zero-order-hold interpolation synchronizes the three sensor timestamps.

In the following, *RIO* refers to our optimization without barometer factor and *BRIO* with it. All flight experiments used *RIO* controller feedback. In addition, we collected data handheld. An experiment starts and ends at the same location

TABLE I: Summary of experiments. The mode describes the experiment settings. H: Handheld, F: Flying

Scenario	No.	Mode	Length [m]	Maximum Velocity [m s ⁻¹]	Median Detections [1]	Moving Objects [1]	Final Position Drift [m]	XY-Position Drift [m]	Position Drift per Distance [%]	Final Yaw Drift [°]	Yaw Drift per Distance [° m ⁻¹]
Urban Night	01	RIO-H	179.7	1.82	15	0	3.54	1.48	1.97	-0.79	-0.004
		BRIO-H	184.7	1.83	15	0	1.42	1.41	0.77	-0.67	-0.004
	02	RIO-H	151.5	1.95	14	0	3.35	0.98	2.21	-1.70	-0.011
		BRIO-H	156.5	1.96	14	0	0.89	0.80	0.57	-1.70	-0.011
	03	RIO-H	153.9	1.82	13	0	3.09	2.29	2.00	2.11	0.014
		BRIO-H	157.5	1.83	13	0	2.39	2.36	1.52	2.76	0.018
04	RIO-H	156.4	1.79	15	1	3.24	0.81	-2.07	1.56	0.010	
	BRIO-H	163.5	1.80	15	1	1.14	1.08	0.70	1.50	0.009	
05	RIO-F	160.0	1.91	10	1	5.35	5.31	3.34	9.03	0.056	
	BRIO-F	166.9	1.91	10	1	5.27	5.26	3.16	8.31	0.050	
06	RIO-F	157.0	1.78	11	2	4.79	4.57	3.05	8.94	0.057	
	BRIO-F	162.4	1.81	11	2	4.78	4.77	2.94	8.59	0.053	
07	RIO-F	185.4	1.62	11	0	4.36	4.09	2.35	8.98	0.048	
	BRIO-F	194.9	1.62	11	0	4.41	4.27	2.26	8.69	0.045	
Forest Path	08	RIO-H	477.6	2.03	8	1	7.50	2.54	1.57	1.56	0.003
		BRIO-H	480.3	2.07	8	1	2.77	2.52	0.58	1.15	0.002
	09	RIO-H	125.1	1.87	6	2	0.48	0.46	0.38	0.55	0.004
		BRIO-H	126.4	1.90	6	2	0.77	0.50	0.61	0.57	0.005
	10	RIO-H	099.4	1.97	5	1	3.20	0.54	3.21	0.80	0.008
		BRIO-H	101.5	2.00	5	1	0.51	0.46	0.50	0.94	0.009
11	RIO-F	487.4	1.98	7	0	17.19	15.00	3.53	12.41	0.025	
	BRIO-F	492.8	1.97	7	0	13.56	13.56	2.75	11.80	0.024	
12	RIO-F	487.5	2.24	6	0	13.23	12.83	2.71	7.56	0.016	
	BRIO-F	490.4	2.25	6	0	11.77	11.37	2.40	6.58	0.013	
Flat Field	13	RIO-F	198.9	2.54	6	0	4.55	3.50	2.29	5.63	0.028
		BRIO-F	202.7	2.62	6	0	3.43	3.23	1.69	6.08	0.030
14	RIO-F	295.2	2.08	9	3	7.15	6.99	2.42	8.57	0.029	
	BRIO-F	299.0	2.08	9	3	5.93	5.92	1.98	8.32	0.028	
Tree Slalom	15	RIO-F	159.2	2.37	8	0	3.56	0.64	2.24	4.30	0.027
		BRIO-F	161.9	2.37	8	0	0.74	0.59	0.46	4.0	0.029

with an accuracy of approximately 2 cm and 2° in the heading to compute the final drift. Table I summarizes all experiments, with numerical values obtained by rerunning the algorithm on collected raw sensor data.

A. Exceptional Robustness

Our main result is the outstanding robustness of radar navigation. Unlike vision or lidar, radar measures velocities, avoiding feature tracking failures that cause state estimation divergence and crashes. Seven handheld experiments (20 min total) and eight flights (35 min total) without failure demonstrate this robustness. *RIO* in the control loop shows sufficient latency and smoothness.

The median number of detected points per scan drops in natural forests compared to urban environments. The urban environment has more objects with high radar cross section (RCS), such as the window frames in Fig. 1a. However, detections from trees or the ground are generally sufficient to estimate the body velocity. Fig. 7 shows accumulated point clouds for different environments. *Urban Night* (Fig. 7a) and *Tree Slalom* (Fig. 7c) have points distributed in elevation, while *Forest Path* (Fig. 7b) is mostly flat with occasional tree trunks. This demonstrates robustness in geometrically degenerate environments where lidar-inertial odometry can fail. Additionally, Fig. 7a shows multipath detections on the stairs and Fig. 7b a pedestrian detection. Both leave the estimate unaffected, highlighting the robustness of the selected Welsch bearing Doppler loss.

B. Performance Overview

Fig. 8a reports less than 1% start-to-end drift in *BRIO* handheld experiments and 2% to 3% in *RIO* and *BRIO*

flights. The state estimate performs consistently across environments (Fig. 8b). The best result, 0.5% drift over a 162 m trajectory, was in the *Tree Slalom 15 BRIO-F* experiment. The results align with other state-of-the-art RIO estimators [6, 12]. Well-tuned visual-inertial odometry (VIO) estimators report drift as low as 0.3% [2] but are vulnerable to poor lighting conditions, as in *Urban Night* (Fig. 4a).

Barometry significantly reduces vertical drift (Fig. 8c). However, its influence on total xyz-drift (Fig. 8a) depends on the horizontal drift magnitude. Handheld experiments mostly drift vertically. Thus the barometer cuts total drift from 2% to almost 0.5%. Flights are dominated by horizontal drift (Fig. 8d). Hence, total drift remains between 2% to 3%.

C. Discussion: Vibrations Leading to Horizontal Flight Drift

Fig. 8d shows that the horizontal drift increases from 0.5% to almost 2.5% when comparing handheld to flown experiments. We attribute this error to gyroscope scale error introduced by platform vibrations [28, p. 49]. Fig. 8e shows that there is a 0.03° m⁻¹ yaw drift in flight versus 0.01° m⁻¹ handheld. The yaw drift is best seen in the trajectory overview in Fig. 9b, where it causes the flown trajectory estimates to twist inwards on the four left-hand bends, leading to horizontal drift. Our quadcopter design does not dampen the low-cost IMU likely causing vibration rectification [29].

The scale-error possibly also explains the lowest drift in *Tree Slalom 15 BRIO-F*. Fig. 7c shows the slalom flight is dynamic with many changes of directions, causing various vibration modes. These may cause alternating yaw drift, potentially canceling each other out.

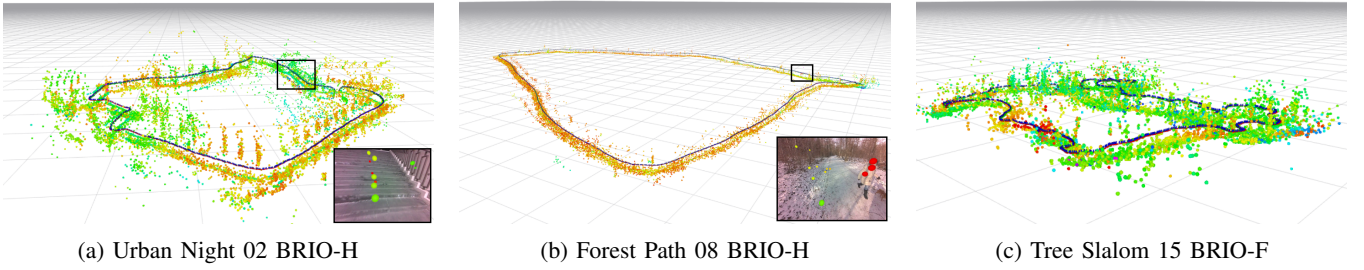


Fig. 7: Isometric view of accumulated point cloud and poses for selected experiments. Grid with 10 m spacing and Doppler point coloring. Photos show three multipath detections on stairs and a pedestrian detection on the forest path (red points).

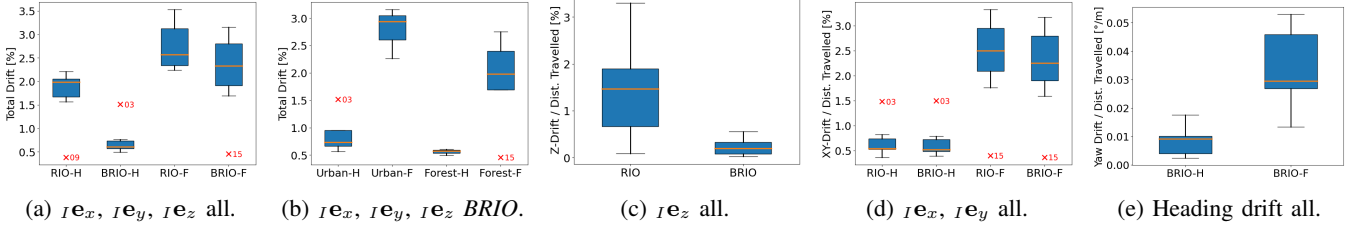


Fig. 8: Start-to-end drift comparison.

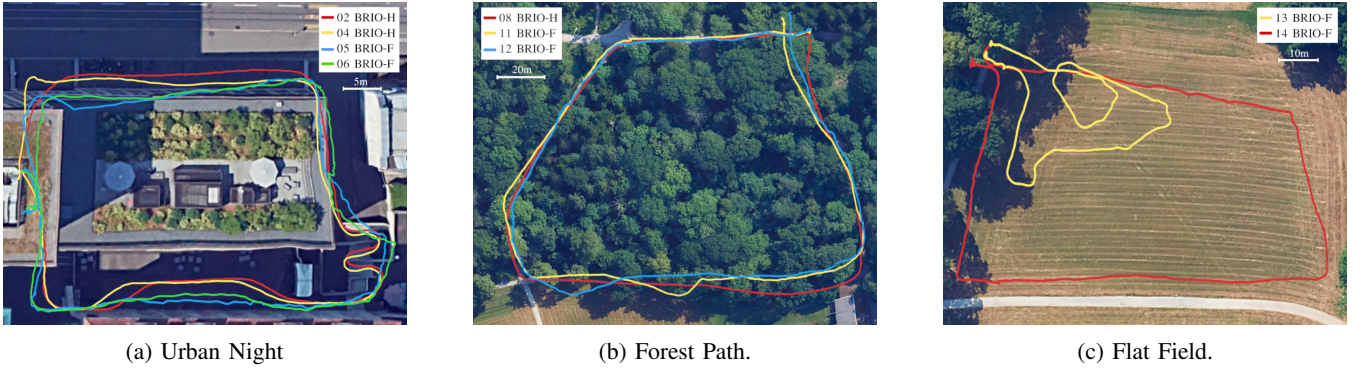


Fig. 9: Satellite image trajectory overlay. Trajectories are manually aligned.

VI. BENCHMARK ON COLORADAR DATASET

We compare *Our* approach to *x-RIO* [9] on the ColoRadar dataset [30]. *x-RIO*, configured with a single radar and without Manhattan assumption, required modifying 16 radar prefiltering parameters for compatibility. Notably, *Ours* only needs the Doppler standard deviation, which we kept unchanged. Both approaches used different IMUs, so we adjusted the IMU parameters to match the ColoRadar dataset. Barometer support was omitted as it is not provided in the dataset. We calibrated the gyroscope turn-on-bias for both approaches using each sequence’s first 3 s.

We evaluate relative pose error (RPE) [31], split into translational and rotational root-mean-square error (RMSE), and the final XY-Position and yaw drift normalized by distance. Table II shows similar performance between the approaches. *x-RIO* slightly outperforms in rotational RPE but exhibits strong terminal yaw drift in most datasets. We suspect their precise binary outlier filtering leads to better estimates, but any false positive induces inconsistencies, such as a wrong yaw rate. *Our* system, with smooth outlier rejection and fixed yaw rate bias, performs consistently well.

Comparing our dataset and ColoRadar’s, our algorithm’s final XY-position drift is better in our handheld experiments

TABLE II: ColoRadar Dataset Results

Dataset	Pipeline	RPE (RMSE)		Final Drift per Distance	
		Trans. [%]	Rot. [°]	XY [%]	Yaw [° m ⁻¹]
hallways_0	x-RIO	4.41	0.39	2.80	0.031
	Ours	4.97	0.91	4.59	-0.066
arpg_1	x-RIO	3.36	0.48	8.28	0.752
	Ours	2.88	0.98	2.81	0.096
aspen_0	x-RIO	3.15	0.37	2.47	0.288
	Ours	3.02	1.13	3.79	0.038
army_2	x-RIO	3.73	0.41	3.97	0.017
	Ours	3.63	1.10	0.76	-0.025
classroom_0	x-RIO	6.92	0.51	4.73	0.116
	Ours	4.28	1.52	1.68	-0.006
outdoors_0	x-RIO	3.19	0.37	1.45	0.128
	Ours	3.19	1.09	1.55	0.007

(0.36 % to 1.49 %) than in theirs (0.76 % to 4.59 %). Our hardware likely has a better extrinsic calibration and more suitable, i.e., restrictive, CFAR configuration.

VII. KNOWN LIMITATIONS

Despite the robustness and performance demonstrated, the proposed estimator has a few known limitations.

Fixed chirp configuration limits the radar’s range and velocity. To address this, we restricted the quadcopter’s maximum input velocity v_{ref} to 2 m s^{-1} and kept the radar within structure range. Larger velocities or distances would require online chirp adaptation, reducing radial velocity resolution.

Ambient pressure bias changes are ignored. Abrupt temperature changes, like moving indoors to outdoors, can cause altitude jumps. One solution is resetting the altitude offset or integrating absolute height or temperature measurements.

Extrinsic calibration is inferred from CAD. However, bearing biases still cause noticeable estimation errors. Calibrating additional effects, such as gravity constant, phase biases, or sensor discretization, will enhance future performance.

Yaw rate offset and scale are hardly observable. Improved yaw observation and vibration management would reduce drift, especially under vibration.

Zero-velocity detection tracking before take-off and after landing requires at least one repeatable CFAR detection. Otherwise, the estimator relies on IMU readings and drifts.

VIII. CONCLUSION

This work presents an open-source m-estimator for baro-radar-inertial odometry. The estimator is robust to moving objects, ghost targets, and aerodynamic disturbances. Radar-stabilized quadcopter flights in human-made and natural environments show its general applicability for multirotor navigation. Accumulated drift as low as 0.5% per distance traveled and robustness in visually and geometrically degraded and dynamic environments highlight the potential of radar to replace lidar or vision-based navigation in GNSS-denied environments. A benchmark shows that our m-estimator has fewer tuning variables and performs more consistently than the *x-RIO* Kalman filter, which uses binary outlier rejection. Future work may investigate DoA accuracy, vibration management, and yaw observability.

REFERENCES

- [1] T. Roucek, M. Pecka, P. Cizek, T. Petricek, J. Bayer, V. Šalansky, T. Azayev, D. Hert, M. Petrлік, T. Báca *et al.*, “System for multi-robotic exploration of underground environments CTU-CRAS-NORLAB in the DARPA Subterranean Challenge,” *Field Robotics*, vol. 2, 2022.
- [2] T. Qin, P. Li, and S. Shen, “Vins-mono: A robust and versatile monocular visual-inertial state estimator,” *IEEE Trans. Robotics*, vol. 34, no. 4, pp. 1004–1020, 2018.
- [3] N. Hudson, F. Talbot, M. Cox, J. Williams, T. Hines, A. Pitt, B. Wood, D. Frousheger, K. L. Surdo, T. Molnar *et al.*, “Heterogeneous ground and air platforms, homogeneous sensing: Team CSIRO Data61’s approach to the DARPA subterranean challenge,” *Field Robotics*, vol. 2, 2022.
- [4] S. Khattak, F. Mascarich, T. Dang, C. Papachristos, and K. Alexis, “Robust thermal-inertial localization for aerial robots: A case for direct methods,” in *Int. Conf. Unmanned Aircr. Syst.*, 2019, pp. 1061–1068.
- [5] C. Waldschmidt, J. Hasch, and W. Menzel, “Automotive radar—From first efforts to future systems,” *IEEE J. Microwav.*, vol. 1, no. 1, pp. 135–148, 2021.
- [6] C. Doer and G. F. Trommer, “An EKF based approach to radar inertial odometry,” in *IEEE Int. Conf. Multisensor Fusion Integration Intell. Syst.*, 2020, pp. 152–159.
- [7] K. Yokoo, S. Beauregard, and M. Schneider, “Indoor relative localization with mobile short-range radar,” in *IEEE 69th Veh. Technol. Conf.*, Spring 2009, pp. 1–5.
- [8] D. Kellner, M. Barjenbruch, J. Klappstein, J. Dickmann, and K. Dietmayer, “Instantaneous ego-motion estimation using Doppler radar,” in *16th Int. IEEE Conf. Intell. Transp. Syst.*, 2013, pp. 869–874.
- [9] C. Doer and G. F. Trommer, “x-RIO: Radar Inertial Odometry with Multiple Radar Sensors and Yaw Aiding,” *Gyrosc. Navig.*, vol. 12, pp. 329–339, Feb. 2022.
- [10] J.-T. Huang, R. Xu, A. Hinduja, and M. Kaess, “Multi-Radar Inertial Odometry for 3D State Estimation using mmWave Imaging Radar,” *arXiv:2311.08608*, 2023.
- [11] J. Michalczyk, R. Jung, and S. Weiss, “Tightly-coupled EKF-based radar-inertial odometry,” in *IEEE/RSJ Int. Conf. Intell. Robots Syst.*, 2022, pp. 12 336–12 343.
- [12] J. Michalczyk, R. Jung, C. Brommer, and S. Weiss, “Multi-state tightly-coupled EKF-based radar-inertial odometry with persistent landmarks,” in *IEEE Int. Conf. Robotics Automat.*, 2023, pp. 4011–4017.
- [13] V. Kubelka, E. Fritz, and M. Magnusson, “Do we need scan-matching in radar odometry?” *arXiv:2310.18117*, 2023.
- [14] M. Jankiraman, *FMCW radar design*. Artech House, 2018.
- [15] A. Kramer and C. Heckman, “Radar-inertial state estimation and obstacle detection for micro-aerial vehicles in dense fog,” in *Exp. Robotics: 17th Int. Symp.* Springer, 2021, pp. 3–16.
- [16] A. Kramer, C. Stahoviak, A. Santamaria-Navarro, A.-A. Agha-Mohammadi, and C. Heckman, “Radar-inertial ego-velocity estimation for visually degraded environments,” in *IEEE Int. Conf. Robotics Automat.*, 2020, pp. 5739–5746.
- [17] K. Harlow, H. Jang, T. D. Barfoot, A. Kim, and C. Heckman, “A new wave in robotics: Survey on recent mmWave radar applications in robotics,” *arXiv:2305.01135*, 2023.
- [18] F. Dellaert and M. Kaess, “Factor graphs for robot perception,” *Found. Trends® Robotics*, vol. 6, no. 1-2, pp. 1–139, 2017.
- [19] W. J. Rey, *Introduction to robust and quasi-robust statistical methods*. Springer Sci. & Bus. Media, 2012.
- [20] NASA Glenn Research Center, “Earth atmosphere model - metric units,” <https://www.grc.nasa.gov/www/k-12/airplane/atmosmet.html>.
- [21] J. Parviainen, J. Kantola, and J. Collin, “Differential barometry in personal navigation,” in *IEEE/ION Position, Location Navig. Symp.*, 2008, pp. 148–152.
- [22] C. Forster, L. Carlone, F. Dellaert, and D. Scaramuzza, “IMU preintegration on manifold for efficient visual-inertial maximum-a-posteriori estimation,” in *Robotics: Sci. Syst.*, 2015.
- [23] I. Dryanovski, “imu_tools/imu_filter_madgwick,” https://github.com/CCNYRoboticsLab/imu_tools.git, 2010.
- [24] J. Sola, J. Deray, and D. Atchuthan, “A micro Lie theory for state estimation in robotics,” *arXiv:1812.01537*, 2018.
- [25] F. Dellaert and GTSAM Contributors, “borglab/gtsam,” <https://github.com/borglab/gtsam>, May 2022.
- [26] M. Kaess, H. Johannsson, R. Roberts, V. Ila, J. J. Leonard, and F. Dellaert, “iSAM2: Incremental smoothing and mapping using the Bayes tree,” *Int. J. Robotics Res.*, vol. 31, no. 2, pp. 216–235, 2012.
- [27] V. Indelman, S. Williams, M. Kaess, and F. Dellaert, “Information fusion in navigation systems via factor graph based incremental smoothing,” *Robotics Auton. Syst.*, vol. 61, no. 8, pp. 721–738, 2013.
- [28] B. Braun, “High performance kalman filter tuning for integrated navigation systems,” Ph.D. dissertation, Technische Universität München, 2016.
- [29] L. Pham and A. DeSimone, “Vibration Rectification in MEMS Accelerometers,” Analog Devices, Tech. Rep., 2017.
- [30] A. Kramer, K. Harlow, C. Williams, and C. Heckman, “Col-oradar: The direct 3D millimeter wave radar dataset,” *Int. J. Robotics Res.*, vol. 41, no. 4, pp. 351–360, 2022.
- [31] M. Grupp, “evo: Python package for the evaluation of odometry and slam,” <https://github.com/MichaelGrupp/evo>, 2017.
- [32] “MMWAVE SDK User Guide,” Texas Instruments Inc., Tech. Rep., 2022.

A. LIST OF SYMBOLS

I	Inertial frame
$I\mathbf{e}_x$	Inertial frame x-axis
$I\mathbf{e}_y$	Inertial frame y-axis
$I\mathbf{e}_z$	Inertial frame z-axis
B	Body frame
$B\mathbf{e}_x$	Body frame x-axis
$B\mathbf{e}_y$	Body frame y-axis
$B\mathbf{e}_z$	Body frame z-axis
R	Radar frame
$R\mathbf{e}_x$	Radar frame x-axis
$R\mathbf{e}_y$	Radar frame y-axis
$R\mathbf{e}_z$	Radar frame z-axis
\mathcal{X}_k	Set of all estimated states up to time k
\mathcal{X}_k^{MAP}	Set of MAP state estimates up to time k
\mathbf{x}	State vector
\mathbf{T}_{IB}	Robot pose
\mathbf{R}_{IB}	Robot orientation
\mathbf{t}_{IB}	Robot translation
\mathbf{v}_{IB}	Robot linear velocity
$\mathbf{R}\mathbf{v}_{IR}$	Radar linear velocity in radar frame
$\mathbf{I}\mathbf{v}_{IR}$	Radar linear velocity in inertial frame
$B\mathbf{b}_g$	Gyroscope bias
$B\mathbf{b}_a$	Accelerometer bias
\mathcal{T}_k	Set of all estimated zero-velocity track positions up to time k
\mathbf{t}	Zero-velocity track
\mathbf{t}_{IT}	Tracked zero-velocity detection position
\mathcal{Z}_k	Set of all measurements up to time k
\mathcal{R}	Set of all radar detections in a frame
T	Radar detection
$R\mathbf{e}_T$	Radar detection bearing vector
$R\mathbf{t}_{RT}$	Radar detection position vector
v_T	Radar detection Doppler velocity
SNR_T	Radar detection SNR
w_T	Radar detection noise
α	Radar detection bearing vector bias
\mathcal{I}	Set of all IMU measurements between two radar frames
$B\boldsymbol{\omega}_{IB}$	Robot angular velocity
$B\mathbf{a}_B$	Robot linear acceleration
\mathcal{B}	Set of barometer measurements
z_p	Barometer height measurement
p	Barometer pressure measurement
\mathcal{K}_k	Set of all radar frames up to time k
\mathcal{K}_j	Set of all radar frames containing track j
\mathcal{L}_k	Set of all zero-velocity tracks up to time k
i	Time index
j	Zero-velocity track index
k	Most recent time index
m	Detection in radar frame index
ρ	Robust loss function
\mathbf{r}_I	IMU factor residual
\mathbf{r}_T	Zero-velocity track factor residual
\mathbf{r}_D	Doppler factor residual
\mathbf{r}_B	Barometer factor residual
\mathbf{r}_P	Prior factor residual
$\mathbf{r}_{\mathbf{R}_{IB}}$	Prior orientation factor residual
$\mathbf{r}_{\mathbf{t}_{IB}}$	Prior position factor residual
$\mathbf{r}_{\mathbf{v}_{IB}}$	Prior linear velocity factor residual
$\mathbf{r}_{B\mathbf{b}_g}$	Prior gyro bias factor residual
$\mathbf{r}_{B\mathbf{b}_a}$	Prior accelerometer bias factor residual
\mathbf{T}_{BR}	Radar extrinsic calibration
\mathbf{R}_{BR}	Radar calibration rotation

$B\mathbf{t}_{BR}$	Radar calibration translation
Σ_P	Prior measurement covariance matrix
Σ_I	IMU measurement covariance matrix
Σ_T	Zero-velocity track position measurement covariance matrix
Σ_D	Doppler measurement covariance
Σ_B	Barometer measurement covariance
σ_D	Doppler measurement standard deviation
σ_B	Barometer measurement standard deviation
\mathbf{v}_{ref}	Velocity control input

B. RADAR CONFIGURATION

AWR1843AOPEVM radar configuration using the Texas Instruments mmWave SDK [32].

```

1 % Created for SDK ver:03.06
2 % Created using Visualizer ver:3.6.0.0
3 % Frequency:77
4 % Platform:xWR18xx_AOP
5 % Scene Classifier:best_vel_res
6 % Azimuth Resolution(deg):30 + 38
7 % Range Resolution(m):0.214
8 % Maximum unambiguous Range(m):10.95
9 % Maximum Radial Velocity(m/s):2.56
10 % Radial velocity resolution(m/s):0.04
11 % Frame Duration(msec):100
12 % RF calibration data:None
13 % Range Detection Threshold (dB):15
14 % Doppler Detection Threshold (dB):15
15 % Range Peak Grouping:enabled
16 % Doppler Peak Grouping:enabled
17 % Static clutter removal:disabled
18 % Angle of Arrival FoV: Full FoV
19 % Range FoV: Full FoV
20 % Doppler FoV: Full FoV
21 sensorStop
22 flushCfg
23 configDataPort 921600 1
24 dfeDataOutputMode 1
25 channelCfg 15 7 0
26 adcCfg 2 1
27 adcbufCfg -1 0 1 1 1
28 profileCfg 0 77 115 7 15 0 0 100 1 64 9142 0 0 30
29 chirpCfg 0 0 0 0 0 0 1
30 chirpCfg 1 1 0 0 0 0 2
31 chirpCfg 2 2 0 0 0 0 4
32 frameCfg 0 2 128 0 100 1 0
33 lowPower 0 0
34 guiMonitor -1 1 1 0 0 0 1
35 cfarCfg -1 0 2 8 4 3 0 15 1
36 cfarCfg -1 1 0 8 4 4 1 15 1
37 multiObjBeamForming -1 1 0.5
38 clutterRemoval -1 0
39 calibDcRangeSig -1 0 -5 8 256
40 extendedMaxVelocity -1 0
41 lvsdStreamCfg -1 0 0 0
42 compRangeBiasAndRxChanPhase 0.0 1 0 1 0 1 0 1 0 1 0 1 0 1
   0 1 0 1 0 1 0 1 0 1 0
43 measureRangeBiasAndRxChanPhase 0 1.5 0.2
44 CQRxSatMonitor 0 3 4 19 0
45 CQSigImgMonitor 0 31 4
46 analogMonitor 0 0
47 aoaFovCfg -1 -90 90 -90 90
48 cfarFovCfg -1 0 0 10.97
49 cfarFovCfg -1 1 -2.49 2.49
50 calibData 0 0 0
51 sensorStart

```